

THE DESIGN, FABRICATION, HYDROSTATIC TEST, AND FAILURE ANALYSIS OF A 610 MM I.D. AS-4/APC-2 RING-STIFFENED [90_n/0] PRESSURE HULL MODEL

Mark A. Lamontia and Mark B. Gruber,
Accudyne Systems, Inc., 134 Sandy Drive, Newark, DE, 19713

ABSTRACT

A 610 mm (24-in) I.D. AS-4/APC-2 ring-stiffened cylinder was designed to demonstrate its hydrostatic pressure load-carrying capability. The cylinder fabrication process combined in situ thermoplastic filament wound 90° plies with tape placed 0° plies, resulting in excellent laminate quality. The cylinder, enclosed with hemispherical steel end closures, was designed to exhibit a strength failure in the shell laminate. In the pressure test, the cylinder collapsed at 37.9 MPa, within 3% of the predicted 39.2 MPa pressure. Shell axial strains exceeded -14,000 μ strain and the shell laminate failed axially away from the hemispherical end closures, between rings 3 and 4. The finite element model was updated with dimensions, properties, and the pre-test geometric shape resulting from process-induced residual stresses. A novel technique accounted for non-linear shear in the material constitutive law. With these enhancements, predicted strains matched test strains within 15%. Four failure criteria were evaluated using the finite element model.

KEY WORDS: Design/Analysis, Resin Materials – Polyetheretherketone, Failure Analysis/
Failure Assessment

1. INTRODUCTION

A program to demonstrate a thermoplastic composite pressure hull model with 610 mm (24-inch) internal diameter was completed. The program goals were to

- demonstrate in situ filament winding for hoop (90°) plies and tape placement for axial (0°) plies as a cost-effective out-of-autoclave process to fabricate the cylinder,
- achieve mechanical stiffness and strength equivalence for the thick cylindrical structure compared with compression-molded flat laminates, and
- minimize weight/displacement ratio of the cylinder.

An additional goal was to demonstrate a mid-length strength-critical failure mode in the cylinder's shell that was not significantly affected by the end closure restraints. For maximum performance, the goal failure would depend on a fiber-dominated strength property.

2. PRESSURE HULL MODEL DESIGN

Figure 2.1 shows the finished pressure hull and Figure 2.2, the model cylindrical geometry. The pressure hull consists of a 16 mm (0.629-inch) thick shell with a 2.27:1 hoop/axial ratio (2.27

times as many 90° plies as 0° plies) and five hoop-wound rings, 12.2 mm (0.49-inch) wide by 36.8 mm (1.45-inch) deep with elliptical fillets. The pressure hull model also incorporates a unique hemispherical end closure design.

The design methodology comprised (1) Preliminary Design of the shell thickness and ring spacing and depth, (2) Detailed Design of the midbay, and (3) Detailed Design of the pressure hull and end closure. A building block program was completed concurrently to confirm design allowables.

2.1 Preliminary Design The pressure hull incorporates 90° rings that partially resist general instability failure, carry some hoop load, but permit potential interbay buckling. The rings themselves are susceptible to lateral instability. With the extra hoop support, the shell is axial-strength critical. How should the design be optimized?

The DAPS (Design and Analysis of Plastic Shells) [1] computer program, specifically modified to account for the brittle failure modes and multiple potential failure locations found in composite stiffened shells, was used in an optimization scheme to adjust dimensions and minimize cylinder weight while maximizing the collapse pressure and maintaining a strength-critical shell failure. Many shell laminate and ring constructions were considered. The shell was defined by its hoop/axial ratio and described in the program with thermo-elastic properties using a 3D lamination code. No knockdown factors were used. The Maximum Stress/Maximum Strain failure criteria were applied to each calculation because cross-ply laminates fail catastrophically following first ply failure when the pressure hull is hydrostatically loaded. Also, those criteria highlight physical failure modes during the design stage. The shell thickness, ring spacing, and ring depth in Figure 2.2 resulted.



Figure 2.1 The APC-2/AS-4 ring-stiffened cylinder had a $[90^{\circ}_{2.27}/0^{\circ}]_n$ laminate stacking sequence and five integral 90° ring stiffeners.

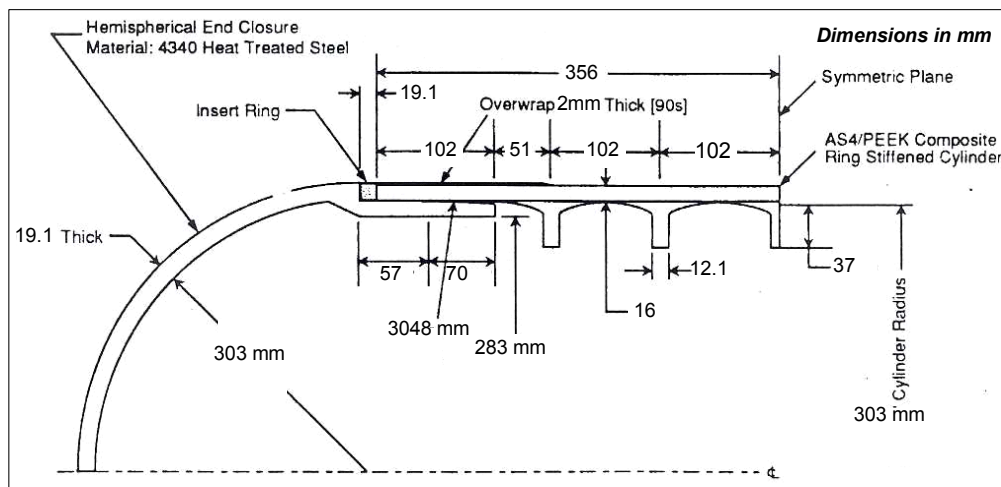


Figure 2.2 The cylinder featured a 2.27:1 hoop/axial ratio shell, five integral all-90° rings with full elliptical fillets, a 90° overwrap at the shell extension outer diameter, 4340 steel hemispherical end closures with tapered lands, and an insert ring to facilitate load introduction.

With the 2.27: hoop/axial ratio, the hoop stresses are relatively low compared with the axial stresses. This resulted in a shell that is strength critical in the axial direction.

2.2 Detailed Design of Midbay Preliminary design was followed by detailed ABAQUS midbay finite element analysis, as shown in Figure 2.3. The midbay region includes a characteristic shell and ring. Large interlaminar shear strains in the fillet region are shown in Figure 2.4. The sources of this stress concentration were (1) axial strain mismatch between the shell and ring and (2) axial shell bending between the rings. The analysis indicated that the stress concentration could be reduced by minimizing the Poisson's Ratio mismatch between the shell and ring or by incorporating large fillets to reduce local bending deformations; the later approach was adopted and elliptical fillets are visible in Figures 2.2 to 2.4. Ring-fillet interlaminar shear, in conjunction with high axial and hoop compressive stress in the fillet, appeared to be a critical failure mode. The absence of an experimentally validated compression-shear multiaxial failure theory was a technology gap, leading to the development of the building block approach.

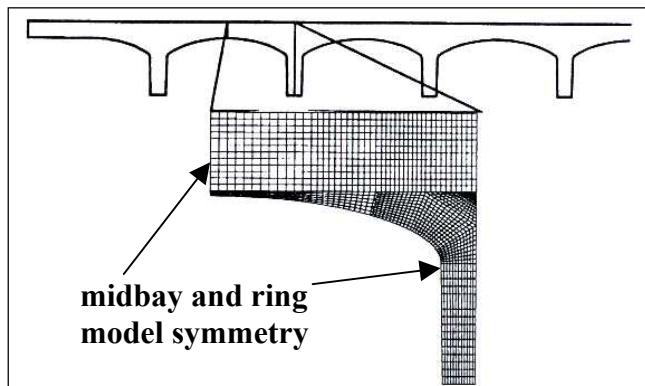


Figure 2.3 ABAQUS was used to complete finite element analyses of stresses, strains, and deflections in the midbay region.

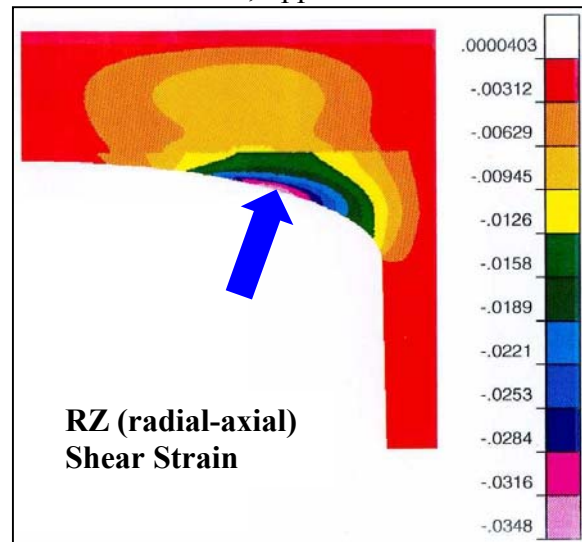
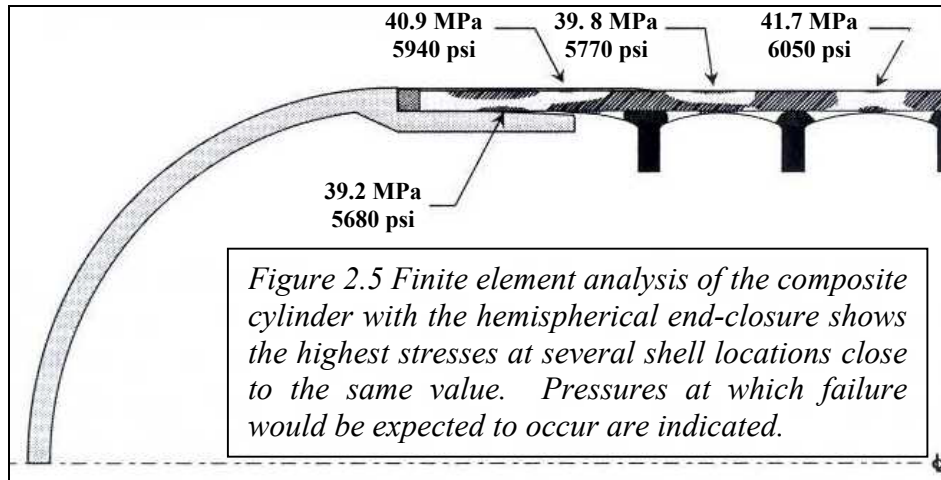


Figure 2.4 An interlaminar R-Z shear strain concentration occurs at the ring-fillet when the cylinder is loaded by hydrostatic compression.

2.3 Detailed Design of Pressure Hull and End Closure The final step in design was to complete the end closure to reduce the end bay stress concentration associated with load introduction. Previously, end closures incorporated flat plates with tapered plug extensions to gradually allow cylindrical shell to closure contact and reduce stress concentrations. However, even the best flat-plate end closures had exceedingly high radial stiffness and the failures would be expected to occur in the ends [2]. Alternatively, under pressure, a hemi-head deflects in the axial and radial directions, steadily reducing its diameter along with the cylinder radial deflection, thus minimizing composite shell bending stresses. As shown in Figure 2.2, a hemispherical design was completed incorporating the best features of the tapered end-plugs and the hemisphere. Additional details to enhance load introduction were

- an insert ring to accommodate shell end rotation,
- additional hoop layers at the inner and outer radii to reduce axial stress concentration,
- incorporation of an anti-brooming lip to prevent undesirable brooming failure.

An example finite element output, Figure 2.5, shows the axial stress and failure pressure at four locations are nearly equal. The minimum predicted collapse pressure is 39.16 MPa (5680 psi).



3. CYLINDER FABRICATION AND PREPARATION FOR TEST

3.1 Cylinder Fabrication The cylinder was fabricated on the innovative collapsible tooling shown in Figure 3.1. The filament winding/tape placement fabrication process [3] in Figures 3.2 and 3.3 is described briefly here. For 90° layers, the filament winding head in Figure 3.2 preheats the underlying bare tool or previously laid laminate with a hot gas. The impregnated tow passing through the head is also preheated to melt. The molten tow and laminate are brought together under a heated shoe. A chilled roller provides a large compaction pressure to compress the void volume as an integral step in refreezing the laminate.



Figure 3.1 Innovative collapsible tooling is used to wind ring-stiffened cylinders.

The tape is creeled on-head for the 0° tape layer, as shown in Figure 3.3. An infrared preheater melts the incoming tape. As with the filament winding head, one of the three main gas torches is aimed directly into the process nip. The compaction roller is shaped like an apple-core to assure uniform contact in the circumferential direction.

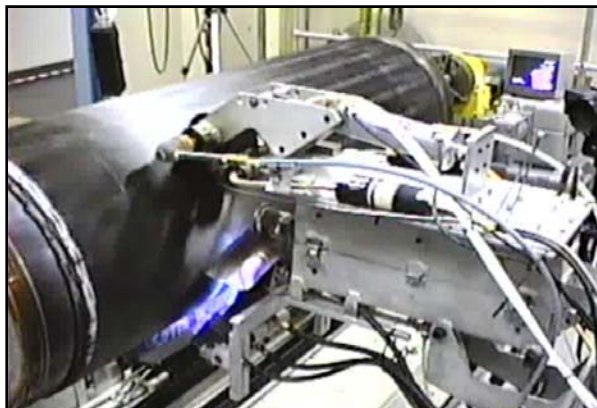


Figure 3.2 Heated filament winding head for hoop (90°) plies.

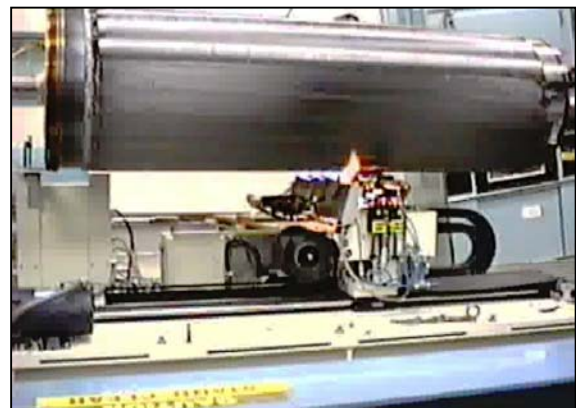


Figure 3.3 Heated tape laying head for 0° plies lies underneath the cylinder on axial ways.

The 610 mm diameter is significant for a filament winding reason: winding back tension cannot be relied upon to achieve laminate consolidation in this size cylinder (or larger). This is characteristically different from winding 178 mm (7-inch) I.D. or smaller cylinders where winding tension can be relied upon to achieve consolidation. All laminate consolidation was achieved with the new process incorporating head mounted consolidation devices [3].

3.2 Cylinder Quality The cylinder filament winding and tape placement processes resulted in excellent cylinder quality with 0.9% V_f , minimal ply undulation, and uniform C-scans [2, 4].

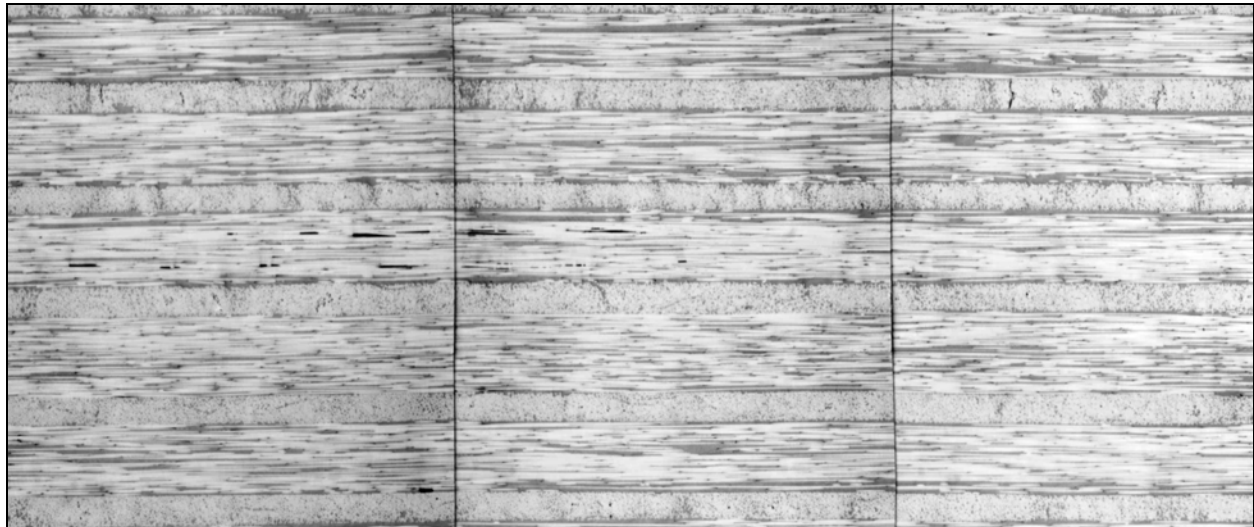


Figure 3.4 Quality was high with a 0.9% void volume fraction, no hoop waviness, and little axial waviness. The ultrasonic C-scan was uniform.

3.3 Building Block Approach Cylinder fabrication followed the testing of 610 mm diameter “building blocks” that quantified design allowables as an integral step in fabrication process development [2]. Building blocks are defined as 610 mm (24-inch) subcomponents manufactured in a manner identical to the pressure hull, but with reduced axial length. They consist of rings, shells, and ring/shell combinations, as shown in Figure 3.5. Individual samples were machined from the building blocks, and tests were developed, enabling the distribution of in situ composite material system properties to be measured; 435 samples were tested.

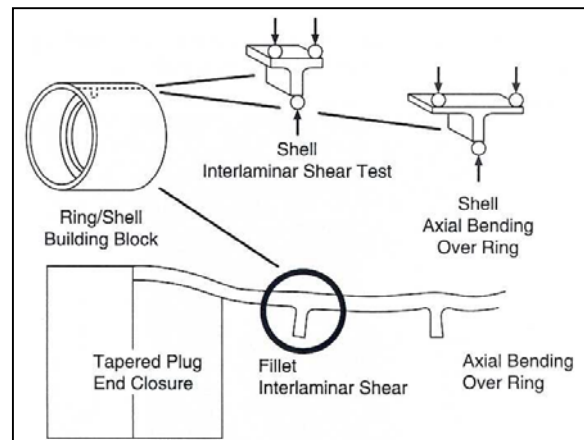


Figure 3.5 Test methods were developed using ring/shell segments cut from wound cylinder building blocks to quantify the severity of the ring/fillet interlaminar shear stress concentration.

Finite element analysis identified shell axial compressive strength and ring fillet interlaminar shear as critical failure modes. Building block test data were able to provide feedback to the design and manufacturing team, supplying design allowables and proving that the full translation of layer properties was demonstrated with the non-autoclave process, as shown in Figure 3.6.

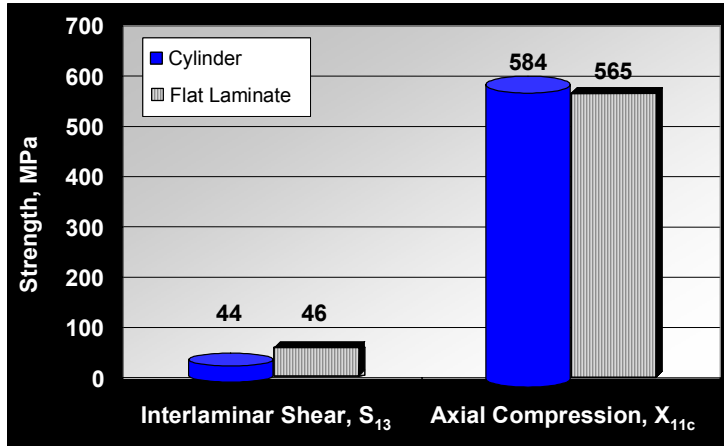


Figure 3.6 A comparison between interlaminar shear and axial compression in building blocks and compression molded flat laminates shows that high strengths are achievable with a high level of consolidation and low layer waviness in the cylinders.

The building block approach was also utilized to quantify the severity of the fillet shear stress concentration shown in Figure 2.4. In the absence of an experimentally validated failure theory for thick-section composites subjected to multiaxial stress states, a 3-point bending test was developed to create the same axial-compression/shear ratio in the critical fillet region as would be experienced in the pressure hull model. Experiments revealed that the ring fillet interlaminar shear was not critical, since catastrophic failure of the specimens occurred at significantly higher loads. Two feasible explanations for this benefit

are (1) synergistic interaction of this multiaxial stress state suppressed failure; or (2) localization occurs but does not propagate and cause significant stress redistribution.

Finally, the building blocks were used to define A-Basis and B-Basis strength allowables for failure prediction. The A- and B-Basis allowables are defined as 99% and 90% probability of survival with a 95% confidence level. With those allowables and the finite element model, Table 3.1 lists failure pressure predictions based upon B-basis allowables, predicting a collapse at 24.7

Location	Failure Mode	MPa	Psi
Shell	Axial Stress	39.2	5680
	<i>R-Z Shear Stress</i>	50.3	7290
Shell End	<i>Axial Stress</i>	44.7	6480
Ring Fillet	<i>R-Z Shear Stress</i>	24.7	3580
End Closure	<i>Ultimate Stress</i>	55.7	8080
Shell	<i>General Instability</i>	58.6	8500

Table 3.1 Expected Failure Modes and Pressures

MPa (3580 psi) due to ring-fillet shear failure, or 39.2 MPa (5680 psi) due to axial shell stress. As our building block approach taught us not to expect fillet shear failure to be catastrophic, the cylinder was predicted to collapse at 39.2 MPa (5680 psi).

4. CYLINDER COLLAPSE TEST AND TEST OBSERVATIONS

The cylinder was instrumented with 204 strain gauges and two acoustic emission sensors, then tested in a high-pressure chamber at NSWC-CD (Naval Surface Warfare Center – Carderock Detachment). It collapsed catastrophically following external hydrostatic pressurization for three hours, finally to 37.92 MPa (5500 psi), within 3% of prediction. Observation of the failed shell and rings indicated that an axial compression failure occurred in the shell laminate between rings 3 and 4, as shown in Figure 4.1. This was corroborated by axial midbay strains that generally exceeded -14000 μ strain as shown in Figure 4.2. There was no evidence of general instability or lateral ring instability; hoop midbay strains shown in Figure 4.3 were nearly equal at less than -7000 μ strain, (gauges 142, 342, 543, 732 mounted circumferentially outside, 242, 442 inside).

Figure 4.4 shows the cumulative acoustic emission counts for the test. Large accumulations



Figure 4.1 In the test, the cylinder failed at 37.9 MPa (5500 psi), within 3% of prediction.

occurred near 26 MPa and 37.9 MPa. Note that this corresponds closely to the test pressures predicted to cause local and global cylinder failure, according to Table 3.1.

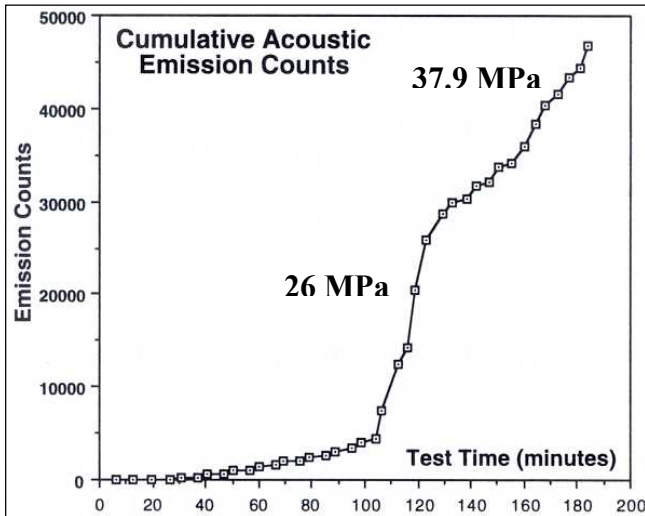


Figure 4.4 Acoustic emission ceased during all but the last two 5-minute pressure holding periods. Large accumulations occurred near 26 MPa and 37.9 MPa.

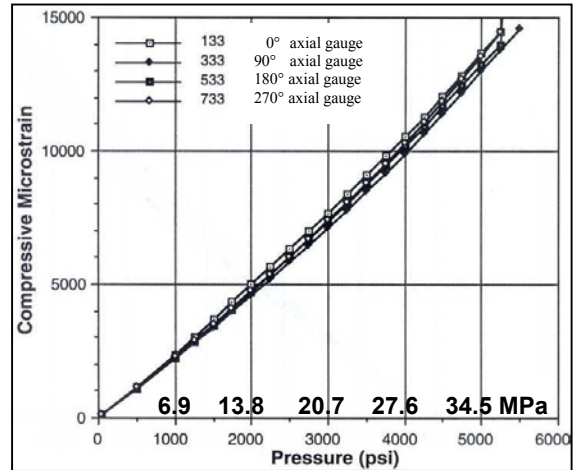


Figure 4.2 Axial strains at Bay 3-4, the midbay were failure initiated, exceeded -14000 μ strain at 3 of 4 locations.

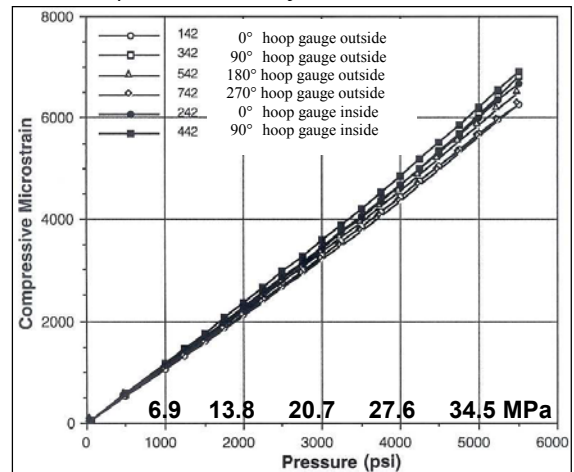


Figure 4.3 Hoop strains at Bay 4-5 approach -7000 μ strain with no evidence of buckling.

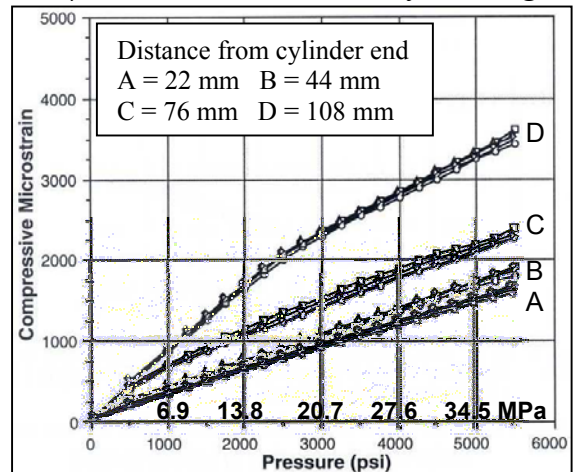


Figure 4.5 End bay hoop strains show the cylinder gradually contacted the hemispherical end closure's tapered land.

Figure 4.5 shows the performance of the cylinder end and hemispherical end closure. Finite element analysis using contact algorithms showed that the cylinder should progressively contact the end closure's 3048 mm radius tapered land shown in Figure 2.2. In Figure 4.5, the hoop oriented strain gauges 22 mm from the cylinder end reached about $-1500 \mu\text{strain}$. The gauges 44 mm from the end reached $-1800 \mu\text{strain}$ as the cylinder continued to radially deflect. At 76 mm and 108 mm from the end, the hoop strains reached -2300 and $-3500 \mu\text{strain}$, respectively. The end closure operated as intended, and reduced the cylinder end stress concentration.

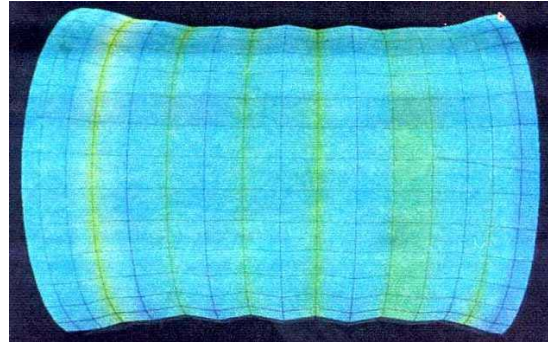


Figure 4.6 shows a cylinder deformed shape with end closures hidden from view. The deformed shape was created by attributing motions proportional to the test strains to the undeformed geometry. As such, the deformed shape is not a model, but an integrated way of showing the experimental cylindrical deflections prior to collapse.

Figure 4.6 The cylinder test deflections, calculated from the strains, show the increased deflection in the mid-bays between each ring.

5. UPDATING THE FINITE ELEMENT MODEL TO ACCURATELY REPRODUCE TEST STRAINS

The failure analysis strategy involved two steps. First, re-employ the cylinder finite element model to more accurately predict the strains measured from the 204 gauges mounted to the cylinder in the hydrostatic collapse test. Second, apply those strains (and stresses) to various failure criteria to quantify each criterion's ability to predict the failure location and test pressure.

Sample finite element model predictions (axial strains) are shown for a midbay/ring combination in Figure 5.1. Figure 5.2 tracks how the finite element model test strain predictions at 34.5 MPa (5000 psi) external loading improved in four modeling phases based on updated material tests or more innovative analyses that included residual stresses and material nonlinearities.

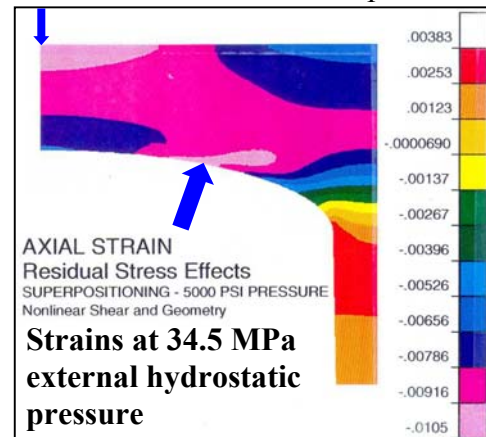


Figure 5.1 Axial strain contour plot for final analysis case at 34.5 MPa (5000 psi) external pressure load.

5.1 Updated Model with Actual Dimensions and Laminate Stacking Sequence The finite element model was first updated to the most accurate possible dimensions and laminate stacking sequence from leftover cylinder end rings and intact fragments from the tested cylinder. Detailed knowledge of the as-manufactured diameters and thickness was in hand, along with the ring thickness. The actual laminate stacking sequence was computed from photomicrographs. Strain results are compared with the test strains in Figure 5.2, bar 1 (“test strains”) and bar 2 (“Updated dimensions and stacking sequence”). There remains disappointing variation after this initial modeling improvement, particularly in O.D. and I.D. midspan axial and hoop strains. The modeled axial strain doesn't reach $-9000 \mu\text{strain}$, while the test axial strain is $-12681 \mu\text{strain}$.

5.2 Updated Model with Actual Ply Modulus The finite element model was next updated with new moduli measured from leftover cylinder end rings and intact fragments from the hydrostatically tested cylinder. The ply modulus based upon the average of these measurements was 122 GPa (17.7 Msi) rather than the 134 GPa (19.5 Msi) originally used. This is the third bar in Figure 5.2, labeled “ply modulus modification – no residual stress effects.” The prediction for the axial midspan strain improves, but overall, a new estimate of modulus did little to close the gaps between predicted and measured strains.

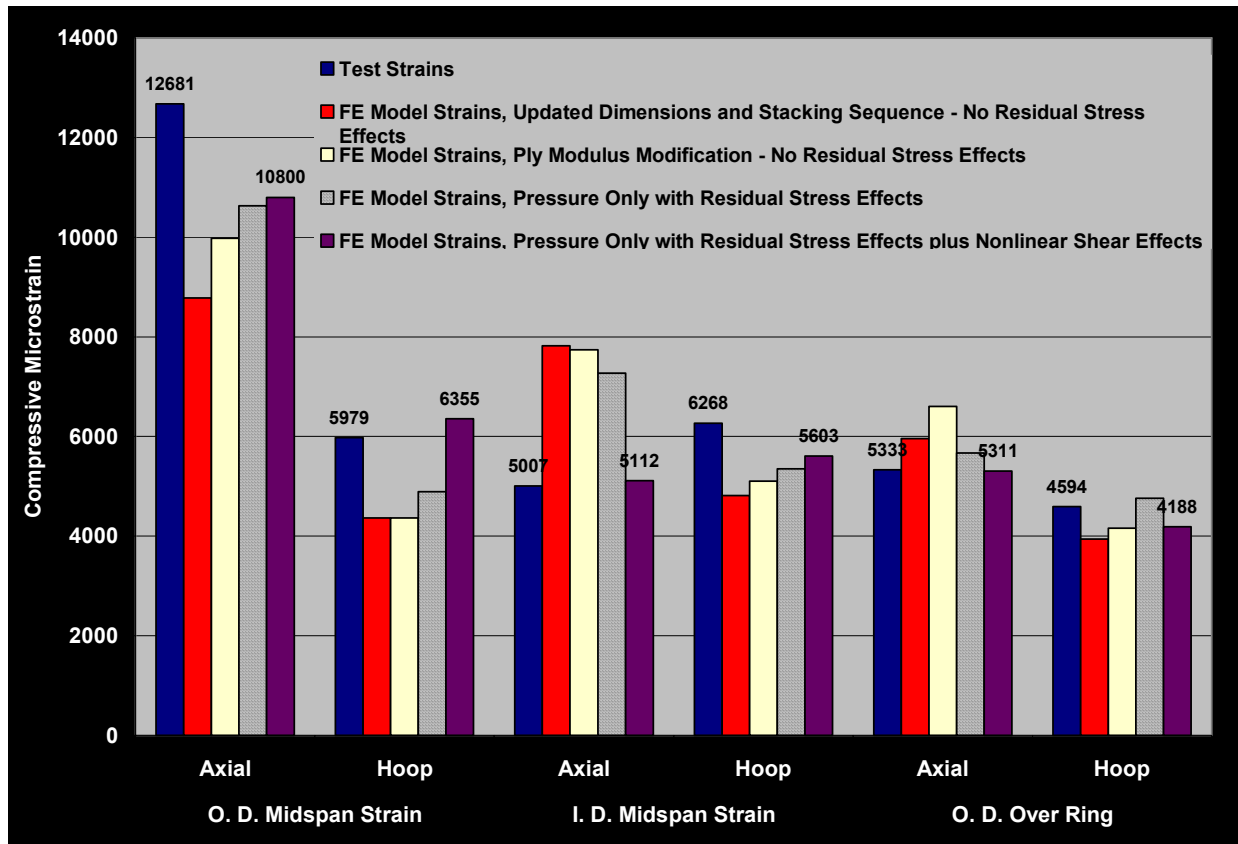


Figure 5.2 Test strains compared with strain predictions from the finite element model, including: 1st bar - test strains, 2nd bar – pressure only with dimension and stacking sequence updated, 3rd bar – additionally with modulus modifications, 4th bar – additionally with residual stress effects, and 5th - additionally with non-linear shear.

5.3 Updated Model with Residual Stresses A critical upgrade to the cylinder finite element model was to account for the initial cylinder shape resulting from residual stresses induced by process cooling. The tested Cylinder (#301) was not available to determine its initial shape, but a similar 610 mm untested ring-stiffened Cylinder (#201) with circular fillets was still intact. Its diameter reduction between ring-stiffeners caused by cooling following the process was measured at 0.25 mm (0.010 inch). Finite element models of Cylinder #201 confirmed that the residual stress modeling approach and the 350°C process temperature reproduced the 0.25mm deflection. When that ΔT was applied to Cylinder #301, the diameter reduction was 0.52 mm (0.021 inch). The larger diametric reduction was caused by the transverse contraction of thin 90° layers at the Cylinder #301 I.D. as the shell cooled. These layers were not wound into Cylinder #201.

Although the reduction in cylinder midbay outer diameter was seemingly small, what did this effect have on the strains? The finite element program was used to calculate the affect of the shrinking and residual stress state on the measured strains. A four-step process was employed:

1. Calculate the cylinder response to pressure without regard to processing.
2. Calculate the cylinder response to a reduction in temperature, starting at the solidification temperature (350°C) and cooling to 25°C. At the end of this analysis step, the cylinder initial shape and residual stress state defines the cylinder to which gauges are applied. That is, as gauges were applied, the cylinder was already responding to residual stresses.
3. Apply the pressure to the cylinder of step 2. This gives the actual strains experienced by the cylinder (residual stresses plus load response), but not those measured by the gauges.
4. Subtract step 2 from step 3 to create a response to pressure load (as seen by the strain gauges), but including the effects of the initial shape caused by residual stresses.

A significant improvement in predicted strain correlation with test strain data was achieved when including this initial shape effect resulting from the process. This in the fourth bar in Figure 5.2 labeled “Pressure only with residual stress effects.”

5.4 Updated Model with Improved Non-linear Material Constitutive Law The final critical upgrade to the cylinder finite element model was to account for the significant material non-linearity in the transverse shear direction on the ply level. An incremental loading strategy was developed whereby piecewise linear increments in the composite material stress-strain response were superimposed throughout the loading history to generate the non-linear shear behavior of the cylinder circumferential ring fillets. An analytic laminated material model was used to compute the tangent or instantaneous effective element constitutive relations for input into ABAQUS. Strain dependent element properties were based upon ply level constitutive relations and are defined using the Ramberg-Osgood equation, as shown in Figure 5.3.

A new code, LAMPATNL, was developed for use with ABAQUS finite element code to incorporate the nonlinear shear stress-strain material properties within the finite element analysis [5]. LAMPTNL generates a stress-strain relationship for any composite ply stiffness (E_{11} , E_{22} , E_{33} , G_{12} , G_{13} , G_{23}). This was used to translate the Iosipescu shear test data into material properties for the finite element analysis.

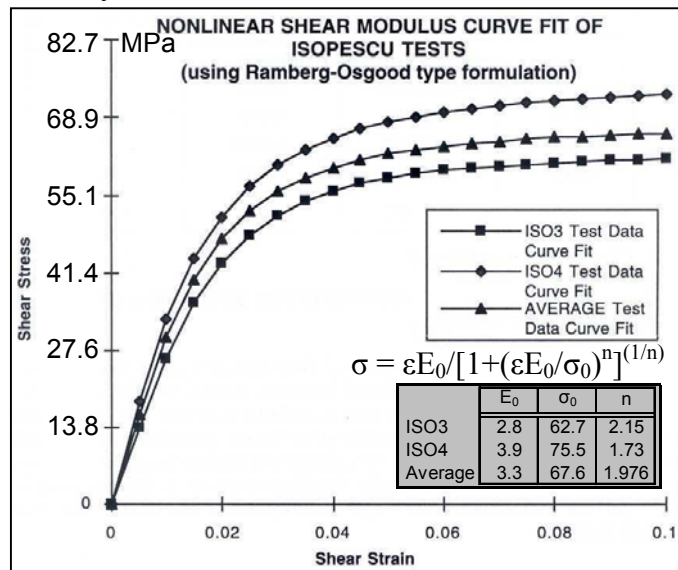


Figure 5.3 Iosipescu shear test curve summary with Ramberg-Osgood curve fits and constitutive law constants.

Using all model improvements (best dimensions, best properties, actual residual stress induced shape, non-linearities), the maximum percentage error for the model predicted strains was 14.8% compared with test strains. This particular single value was higher than hoped for, but as a group the modeled strains fit the data best when considering the other strain values in other directions. Other axial strains were within 2.1%; hoop strains within 10.9%.

6. FAILURE CRITERIA APPLIED TO PREDICTED STRAIN

Four failure criteria were applied to the predicted strains from the cylinder midbay finite element model. It was found that knowledge of the in situ transverse interlaminar shear strength, S_{23} , was critical to the use of each criterion. For each criterion, two different values of the transverse shear strength were evaluated. This section will review the cylinder failure pressure prediction and failure location with the various failure criteria applied.

6.1 Maximum Stress Failure Criterion Figure 6.1 shows the safety factor and failure location for the cylinder midbay when the Maximum Stress Failure Criteria is employed. Figure 6.2 shows the Mode of Failure versus location.

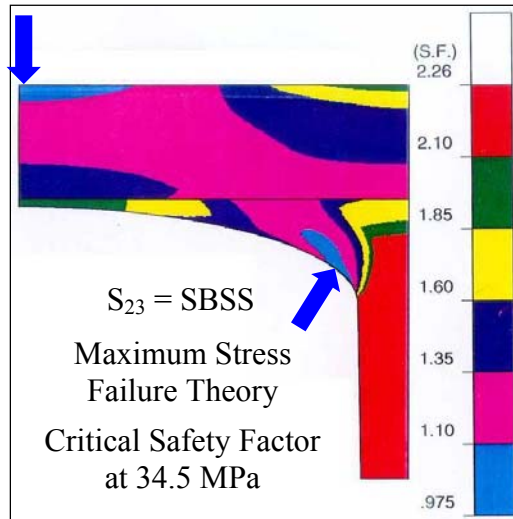


Figure 6.1 Safety Factor versus location for Maximum Stress Failure Criteria when S_{23} = short beam shear strength.

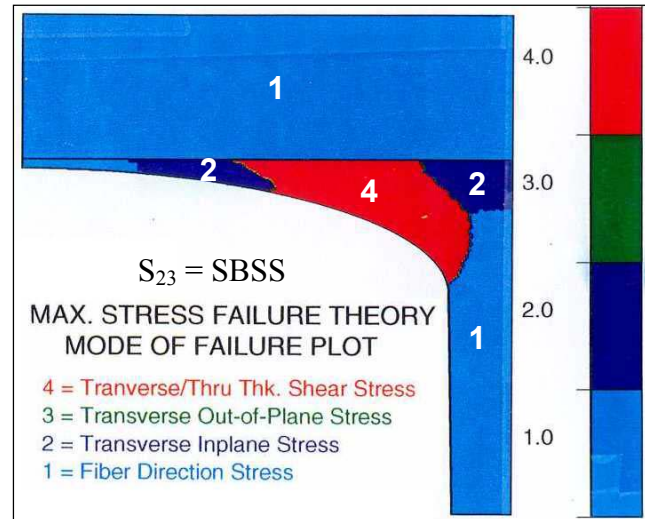


Figure 6.2 The critical failure mode is transverse shear in the fillet region when S_{23} is equal to the short beam shear strength.

The minimum safety factor is 0.975 at the fillet ellipse and the shell O.D. midbay between rings. The 0.975 represents 33.6 MPa (4875 psi) external pressure. This reinforces the contention that fillet shear failure would not represent the critical cylinder collapse.

Figures 6.3 and 6.4 repeat the Maximum Stress Failure Criteria, but the transverse shear is set higher, to one-half the transverse compression strength (close to the value measured from the Iosipescu shear test).

The minimum safety factor is 0.991 at the shell O.D. between rings, representing a 34.2 MPa (4955 psi)

external pressure. This means that collapse is predicted in the correct location at about 10% lower than actual pressure applied in the

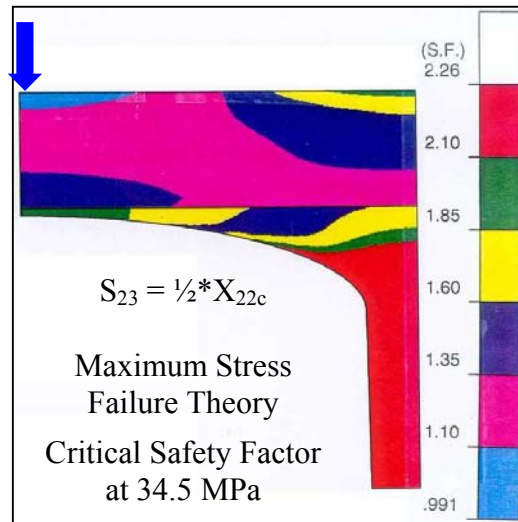


Figure 6.3 Safety Factor versus location for Maximum Stress Failure Criteria when S_{23} is one-half the transverse compression strength.

hydrostatic test. Figure 6.4 shows that with the increased shear strength, the critical mode is at the center of the midbay span O.D. and is fiber direction compression.

6.2 Maximum Strain Failure Criterion Figure 6.5 shows the minimum safety factor for the Maximum Strain Failure Criterion when the transverse shear strength, S_{23} , is equal to one-half the transverse compression strength. The results are similar to Figure 6.3. The safety factor of 1.03 implies a failure pressure of 35.5 MPa (5150 psi), only 6.3% below the actual 37.9 MPa (5500 psi) test pressure. The mode of failure is axial compression.

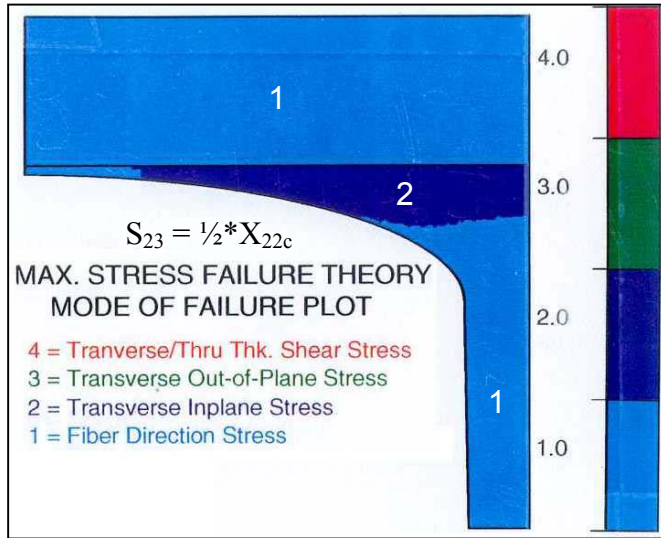


Figure 6.4 The critical failure mode is transverse shear in the fillet region when S_{23} is one-half the transverse compression strength.

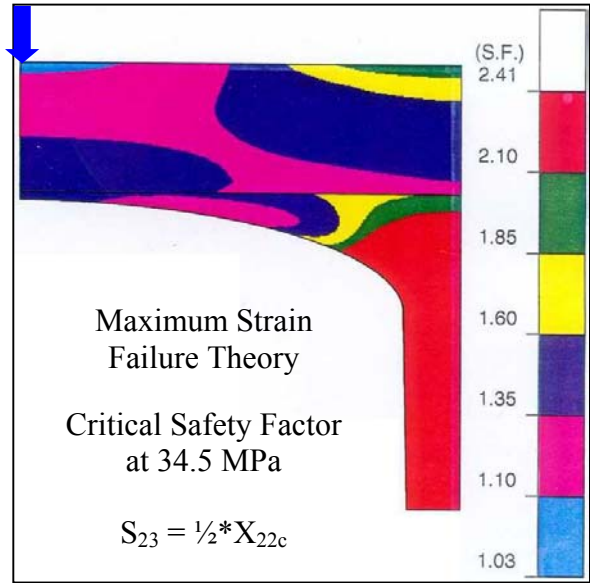


Figure 6.5 Safety Factor versus location for Maximum Strain Failure Criteria when S_{23} is one-half the transverse compression strength. Failure is predicted at 35.5 MPa, 6.3% below test pressure.

6.3 Modified Hashin Failure Criterion The Modified Hashin failure criterion splits the failure of composite lamina into fiber and matrix modes.

The fiber mode is treated as a maximum stress failure mode without interaction terms for the matrix stresses. The matrix directions are evaluated using an interaction criterion based upon whether the matrix stresses are tensile or compressive. For the fiber direction, failure occurs when

$$\frac{\sigma_{11}}{X_{11c}} = 1 \quad (1)$$

For the matrix direction, failure is governed by

$$\left(\frac{\sigma_n}{X_{22t}}\right)^2 + \left(\frac{\tau_{nt}}{S_{23}}\right)^2 + \left(\frac{\tau_{nl}}{S_{12}}\right)^2 = 1 \quad \text{when } \sigma_n > 0 \quad (2)$$

$$\left(\frac{\tau_{nt}}{S_{23}}\right)^2 + \left(\frac{\tau_{nl}}{S_{12}}\right)^2 = 1 \quad \text{when } \sigma_n < 0 \quad (3)$$

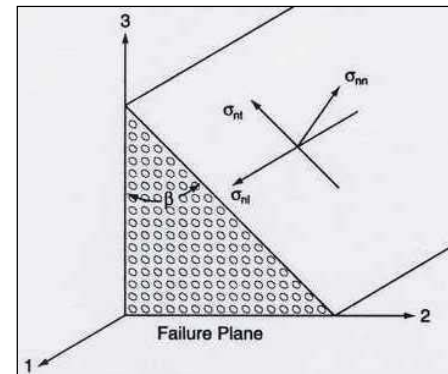


Figure 6.6 β angle for Modified Hashin criterion

where σ_n is the normal stress on the failure plane parallel to the fiber direction and defined by β ,

and τ_{nt} and τ_{nl} are the shear stresses normal σ_n to as shown in Figure 6.6. The Modified Hashin failure criterion is evaluated on all β angle failure planes at each point of interest.

Figure 6.7 shows the minimum safety factor is only 0.575 for the Modified Hashin failure criterion when the transverse shear strength, S_{23} , is equal to the short beam shear strength. This indicates a collapse pressure of only 19.8 MPa (2875 psi), far below the test pressure. Figure 6.8 indicates matrix failure in the critical fillet region. The minimum safety factor rises to 0.991 when the transverse shear strength, S_{23} , is equal to one-half the transverse compression strength, as shown in Figure 6.9. This computes to a collapse pressure of 34.2 MPa (4955 psi), with a fiber mode of failure, as shown in Figure 6.10.

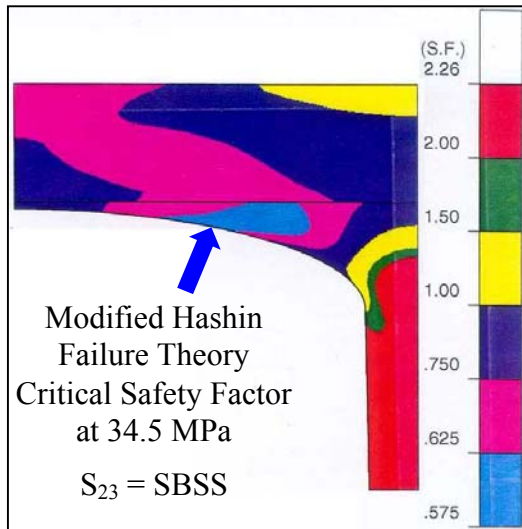


Figure 6.7 Safety Factor vs. location for Modified Hashin Failure Criteria when S_{23} equals short beam shear strength.

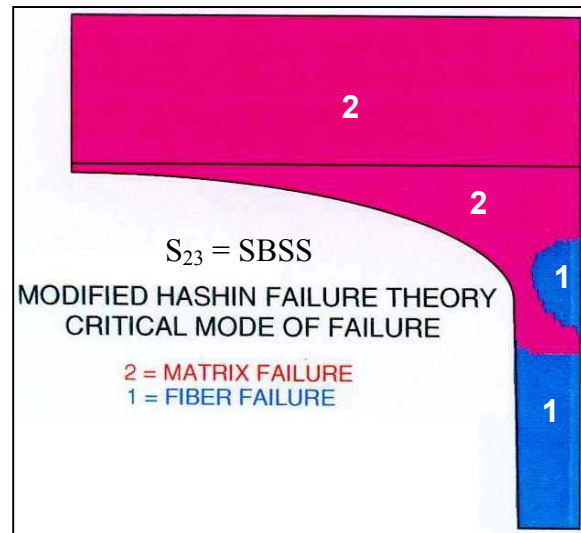


Figure 6.8 The critical failure mode is matrix failure in the fillet region when S_{23} is equal to the short beam shear strength

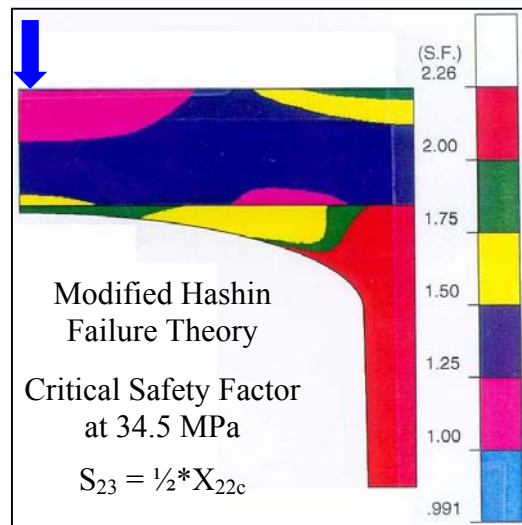


Figure 6.9 Safety Factor vs. location for Modified Hashin Failure Criteria when S_{23} equals one-half the transverse compression strength.

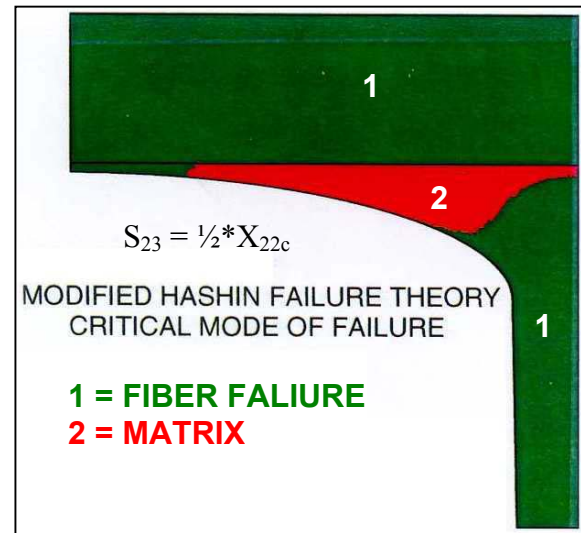


Figure 6.10 The critical failure mode is fiber failure in the fillet region when S_{23} is equal one-half the transverse compression strength.

6.4 Tsai–Wu Interaction Failure Criterion As an additional case, the Tsai-Wu failure criterion was applied to the midbay model when the transverse shear strength, S_{23} , was set equal to one-half the transverse compression strength. Figure 6.11 shows the minimum safety factor is 0.830, more conservative than the Maximum Stress, Maximum Strain, or Modified Hashin failure criteria. The collapse pressure is predicted to be only 28.6 MPa (4150 psi).

Table 6.1 summarizes the failure modes and failure pressures predicted for all four failure modes and two different values for the through-thickness shear strength, S_{23} . When S_{23} was set equal to the short beam shear strength, 35.16 MPa (5.1 ksi), predictions indicated cylinder failure by shear in the fillet for both the Maximum Stress and Modified-Hashin failure criteria. Much better predictions occurred with S_{23} set equal to one-half the axial compression strength, i.e. $\frac{1}{2}X_{22c}$, or 91.7 MPa (13.3 ksi). In that case, the Maximum Stress, the Maximum Strain, and the Modified Hashin criteria all predicted the correct axial midbay O.D. failure location and axial compression failure mode with essentially the same pressure, ranging from 34.16 to 35.51 MPa (4955 to 5150 psi). The higher value is only 6.3% below the actual collapse test pressure.

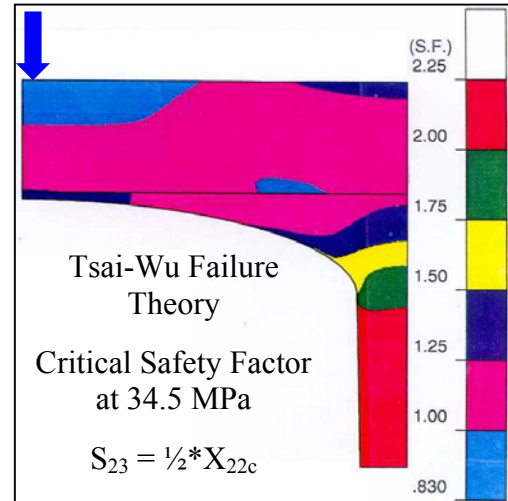


Figure 6.11 Safety Factor versus location for Tsai-Wu Failure Criteria when S_{23} is one-half the transverse compression strength.

It may, in fact, be correct that the failure predictions generated when $S_{23} = SBSS$ are an indication of local failure in the fillet region, and further, that this local failure is associated with the elevation in acoustic emission counts shown in Figure 4.4. Global failure is correctly predicted when S_{23} is higher, more nearly equal the value obtained by Iosipescu shear testing.

Failure Criterion	$S_{23} =$	Failure Location	Failure Mode	Failure Pressure	
				MPa	psi
Maximum Stress	SBSS	Ring fillet	Through thickness shear stress	33.6	4875
Maximum Stress	$\frac{1}{2}X_{22c}$	Axial MidbayOD	Fiber direction stress	34.2	4955
Maximum Strain	$\frac{1}{2}X_{22c}$	Axial MidbayOD	Fiber direction strain	35.5	5150
Modified Hashin	SBSS	Ring fillet	Matrix failure	19.8	2875
Modified Hashin	$\frac{1}{2}X_{22c}$	Axial MidbayOD	Fiber failure	34.2	4955
Tsai-Wu	$\frac{1}{2}X_{22c}$	Axial MidbayOD	no information	28.6	4150

Table 6.1 Summary comparison of predicted failure modes and pressures using the four failure criteria of interest and two values for transverse shear strength ($S_{23} = SBSS$ or $\frac{1}{2}X_{22c}$).

7. CONCLUSIONS

A thick AS-4/APC-2 ring stiffened cylinder was fabricated to demonstrate the in situ filament winding/tape placement process. The cylinder was successfully designed to fail in the shell due to axial stress. In the hydrostatic test, the cylinder failed within 3% of the pre-test prediction. The failure mode was axial collapse away from the hemispherical ends. The “building block

approach” applied in the cylinder development aided establishing design allowables as an integral step in process prove out. For the failure analysis, strain predictions were updated after the test with actual cylinder and ring dimensions, modulus measurements, and new analyses that accounted for (1) residual stresses and the initial pre-test cylinder shape that developed during process cool-down and (2) non-linear shear in the ring fillets. The Maximum Stress and Modified Hashin criteria predicted ring failure when S_{23} was set equal to its test value (ignoring the potential synergistic benefit of compression upon shear). The Maximum Stress, Maximum Strain, and Modified Hashin failure criteria all predicted the correct axial collapse failure when S_{23} was set higher, equal to one-half the shell axial compression strength.

8. ACKNOWLEDGEMENTS

The authors acknowledge the contributions of many co-investigators. Jay Sloan, DuPont Engineering, led the finite element modeling and the failure analysis. Mike Smoot led the cylinder fabrication. Travis Bogetti, U. S. Army Ballistics Research Laboratory, developed the nonlinear material constitutive modeling capability and LAMPAT. Professor Jack Gillespie, University of Delaware, defined the building block tests, consulted throughout the failure analysis, and led the innovative post collapse test material evaluations. Kent Tacey, Dave Bonnani, Wayne Phyllaier, and Bob Rockwell, Naval Surface Warfare Center, Carderock Division, assisted throughout the failure analysis effort. Brian Waibel, Accudyne Systems, created color animations of the cylinder deflection sequence.

9. REFERENCES

- [1] Renzi, J. R., “Axisymmetric Stresses and Deflections, Interbay Buckling, and General Instability of Orthotropic Hybrid Ring-Stiffened Cylindrical Shells under External Hydrostatic Pressure,” Report NSWC TR 80-269, Naval Surface Warfare Center, Silver Spring, MD, April 19, 1981.
- [2] Lamontia, M. A., M. B. Gruber, M. A. Smoot, J. G. Sloan, and J. W. Gillespie, Jr., “Performance of a Filament Wound Graphite/Thermoplastic Composite Ring-Stiffened Pressure Hull Model,” Journal of Thermoplastic Composite Materials, Vol. 8, January 1995, p.15.
- [3] Lamontia, M. A., M. B. Gruber, J. F. Pratte, “The Fabrication and Performance of Ring-stiffened Cylinders Manufactured by a Combined In Situ Automated Thermoplastic Filament Winding and Tape Laying Process,” Proceedings of the 25th Jubilee International SAMPE EUROPE Conference 2004 of the Society for the Advancement of Materials and Process Engineering, Paris EXPO, Porte de Versailles, Paris, France, March 30 – April 1, 2004, p.527.
- [4] Olson, B. D., M. A. Lamontia, J. W. Gillespie, Jr., and T. A. Bogetti, "The Effects and Non-Destructive Evaluation of Defects in Thermoplastic Compression-Loaded Composite Cylinders," Journal of Thermoplastic Composite Materials, Vol. 8, January 1995, p 109.
- [5] Bogetti, T. A., B. P. Burns, and C. P. Hoppel, “LAMPAT: A Software Tool for Analyzing and Designing Thick Laminated Composite Structures,” Army Research Lab - Aberdeen Proving Ground MD, Report Number A357103, September 1995.